
Model Study of the Spinning of Thermotropic Liquid Crystalline Polymers: Fiber Performance Predictions and Bounds on Throughput

M. GREGORY FOREST and HONG ZHOU

Department of Mathematics, University of North Carolina, Chapel Hill, NC 27599-3250

QI WANG

Department of Mathematical Sciences, Indiana University–Purdue University at Indianapolis, Indianapolis, IN 46202

Received: February 2, 1999

Accepted: May 19, 1999

ABSTRACT: We apply a model for thermotropic liquid crystalline polymers (TLCPs) that couples hydrodynamics, anisotropic rodlike microstructural dynamics, free surface effects, and thermodynamics to study fiber spinning of these materials. The model incorporates a Doi type theory for the nematodynamics, along with physical constants, empirical correlations for air drag and functional heat loss coefficient, and rheological relations that are consistent with the melt processing of TLCPs. This new single-phase model (Forest et al., 1998) does not arbitrarily assume a rigid fiber of constant velocity below glass transition temperature of the TLCP, a feature that allows a multiparameter stability calculation of the critical draw ratio. For this study, fiber spinning steady states are computed in experimentally based physical regimes. We predict spun fiber performance properties (birefringence, modulus, and axial force), process sensitivity, and bounds on throughput (draw ratio) due to heat loss, air drag, the temperature variation between the melt and ambient, and the material properties of TLCPs. © 1999 John Wiley & Sons, Inc. *Adv in Polym Techn* 18: 314–335, 1999

Correspondence to: Qi Wang at qwang@math.iupui.edu or tel: 317-274-8144.

Introduction

Isothermal spinning flows of liquid crystalline polymers (LCPs) have been studied by Ramalingam and Armstrong¹ for qualitative features; by Forest, Wang, and Bechtel^{2,3} to include general nematic LCP behavior and stability of spinning states; and by Forest and Ueda⁴ to include an Avrami-based kinetics of crystallization. These studies employed slender 1-D models derived from the 3-D constitutive and flow equations for LCPs due to Bhawe, Menon, Armstrong, and Brown (BMAB).⁵ Here we extend our study to spinning flows of thermotropic LCPs (TLCPs). We model TLCPs by acknowledging both isotropic and anisotropic contributions to stress, as discussed further in this section. The TLCP spin process is simulated with steady-state boundary conditions imposed at fixed upstream and downstream locations. The glass transition temperature is a free boundary, below which the material may be modeled in two ways: traditionally, as a rigid cooling fiber (in spin models of PET and viscoelastic fluid melts,^{6–10} and through a single-phase model developed by Forest, Zhou, and Wang.¹¹

We exhibit that the single-phase model solution smoothly evolves toward a constant velocity downstream when the TLCP is realistically characterized; thus, we remove the arbitrary imposition of a rigid fiber below glass transition temperature. The removal of this arbitrary condition is fundamental: the single-phase model allows us to calculate process stability in the form of the critical draw ratio, and then we compare how material and process parameters affect the maximum stable drawing speed. Standard industry⁶ models and codes are two phase, defying a stability evaluation.

The goal of this article is to apply the TLCP spin model in a realistic physical regime. We employ accepted forms for air drag and a functional heat loss coefficient; we also consider a temperature-dependent, short-range intermolecular potential and incorporate LCP rotary diffusivity. We further incorporate an isotropic stress contribution in the total stress in the constitutive form of BMAB, which we propose to measure experimentally at melt temperatures where the LCP has only an isotropic equilibrium phase.

The article is organized as follows. We first briefly recall the model. We then collect experimentally based material and processing data for TLCPs, nondimensionalize the equations, and identify ap-

proximate values of important parameters and empirical correlations. Finally, we present the numerical fiber spinning solutions and stability results, and benchmark the model against published experimental and industrial reports of nonisothermal fiber spinline behavior.^{6,7,12–14} We note the models of George⁶ and Vassilatos et al.⁷ are Newtonian, nonisothermal; Metzner and Prilutski¹² use an isothermal Doi model, whereas Zieminski and Spruiell¹³ use a nonisothermal Maxwell (isotropic) model with crystallization kinetics; Picken et al.¹⁴ focus on solid fiber properties induced by spinning. Our model incorporates anisotropic nonisothermal behavior, but without crystallization; we infer solid fiber properties (e.g., elastic modulus) as in Picken et al.¹⁴ We emphasize that predictions in the TLCP spinning regime are often dramatically different from the same model in other parameter regimes. From a realistic TLCP spinning regime, we document model predictions for spinline and spun fiber response to material, processing, and empirical parameters.

3-D Model Formulation

The governing equations are given in the following:

Incompressibility condition

$$\nabla \cdot \mathbf{v} = 0 \quad (1)$$

Conservation of momentum

$$\rho \frac{d}{dt} \mathbf{v} = \nabla \cdot \boldsymbol{\tau} + \rho \mathbf{g} \quad (2)$$

where ρ is the density of the polymeric liquid, \mathbf{v} is the velocity vector, $\boldsymbol{\tau}$ is the total stress tensor, $\rho \mathbf{g}$ is the external force due to gravity, and $\frac{d}{dt}(\cdot)$ denotes

the material derivative $\frac{\partial}{\partial t}(\cdot) + \mathbf{v} \cdot \nabla(\cdot)$.

Constitutive equation for stresses:

$$\begin{aligned} \boldsymbol{\tau} &= -p\mathbf{I} + \hat{\boldsymbol{\tau}} \\ \hat{\boldsymbol{\tau}} &= \hat{\boldsymbol{\tau}}_{\text{iso}} + \hat{\boldsymbol{\tau}}_{\text{aniso}} \\ \hat{\boldsymbol{\tau}}_{\text{iso}} &= 2\eta(T)\mathbf{D} \\ \hat{\boldsymbol{\tau}}_{\text{aniso}} &= 3ckT[(1 - N(T)/3)\mathbf{Q} - N(T)(\mathbf{Q} \cdot \mathbf{Q}) \\ &\quad + N(T)(\mathbf{Q} : \mathbf{Q})(\mathbf{Q} + \mathbf{I}/3) + 2\lambda(T)(\nabla \mathbf{v}^t : \mathbf{Q})(\mathbf{Q} + \mathbf{I}/3)] \end{aligned} \quad (3)$$

where \mathbf{D} is the rate-of-strain tensor, \mathbf{Q} is the orientation tensor,² and p is the scalar pressure. In eq. (3), $\eta(T)$ is modeled as the effective isotropic viscosity, presumed to obey an Arrhenius relation,

$$\eta(T) = \eta_0 e^{E/R(1/T - 1/T_0)} \quad (4)$$

where E is the activation energy, R is the gas constant, and η_0 is the effective isotropic viscosity for LCPs at an experimental temperature T_0 above the melting point.

The dimensionless scalar parameter $N(T)$ characterizes the strength of the intermolecular potential, c is the number of polymer molecules per unit volume, and $\lambda(T)$ is the relaxation time of the LCP molecules associated with rotation of the dumbbell molecules, k is the Boltzmann constant, and T is absolute temperature. The value of $N(T)$ is chosen to match the isotropic-to-nematic phase transition at a critical temperature. The anisotropic stress contribution $\hat{\tau}_{\text{aniso}}$ corresponds to orientational stress due to rotary diffusion. For thermotropic LCPs, we propose that η_0 is given by the experimentally determined viscosity of the isotropic melt at temperature T_0 . It seems clear that the high temperature melt, for which $\mathbf{Q} \sim 0$, has a nonzero zero-strain-rate viscosity. An alternative constitutive model for HPC (hydroxypropylcellulose) is discussed in Huang, Magda, and Larson,¹⁵ and related to the stress force discussed by Walker and Wagner.¹⁶ Namely, one can posit a stress relationship for imposed steady shear of the form

$$\hat{\tau} = ckT\lambda\dot{\gamma}f(\mathbf{Q})H(\lambda\dot{\gamma}) \quad (5)$$

where $\dot{\gamma}$ is the shear rate, the scalar function $f(\mathbf{Q})$ is assumed by these authors to depend on the uniaxial order parameter s , and H is an empirical shear thinning function. This stress relation is equivalent for imposed shear to our posited form $\hat{\tau} = \tau_{\text{iso}} + \tau_{\text{aniso}}$ if we identify $\eta_0 \equiv 3ck\lambda\bar{\eta}$, where $\bar{\eta}$ is a parameter with the units of temperature, and use the nematic eq. (8).

We also posit an Arrhenius relation for relaxation time,

$$\lambda(T) = \lambda_0(\mathbf{Q})e^{\omega(1/T - 1/T_0)} \quad (6)$$

where $\lambda_0(\mathbf{Q})$ is the relaxation time of the LCP at the temperature T_0 , and ω is a parameter (units of temperature) to be determined from experiments. We also consider the orientation dependence on rotary diffusivity,¹⁷

$$\lambda_0 = \tilde{\lambda}_0 \left(1 - \frac{3}{2} \mathbf{Q} : \mathbf{Q}\right)^2 \quad (7)$$

Without loss of generality, we select the same experimental temperature T_0 in eqs. (4) and (6), which we later choose as the melt temperature for convenience (i.e., $T_0 = T_{\text{melt}}$). Any other choice of experimental temperatures amounts to a simple rescaling in which the products $\eta_0 e^{-E/(RT_0)}$ and $\lambda_0 e^{-\omega/T_0}$ are independent of T_0 in accordance with these Arrhenius forms.

Orientation tensor equation

$$\begin{cases} \frac{d}{dt} \mathbf{Q} - (\nabla \mathbf{v}^t \cdot \mathbf{Q} + \mathbf{Q} \cdot \nabla \mathbf{v}) = F(\mathbf{Q}) + G(\mathbf{Q}, \nabla \mathbf{v}) \\ F(\mathbf{Q}) = -\sigma_d(T)/\lambda(T) \{ (1 - N/3)\mathbf{Q} - N(\mathbf{Q} \cdot \mathbf{Q}) \\ \quad + N(\mathbf{Q} : \mathbf{Q})(\mathbf{Q} + \mathbf{I}/3) \} \\ G(\mathbf{Q}, \nabla \mathbf{v}) = \frac{2}{3} \mathbf{D} - 2(\nabla \mathbf{v}^t : \mathbf{Q})(\mathbf{Q} + \mathbf{I}/3) \end{cases} \quad (8)$$

Here, $\sigma_d(T)$ is a dimensionless parameter describing the anisotropic drag that a molecule experiences as it moves relative to other polymers: $0 < \sigma_d \leq 1$, where $\sigma_d = 1$ is the isotropic friction limit and $\sigma_d = 0$ is the highly anisotropic limit. Note that F characterizes the orientation dynamics independent of flow, whereas G describes the flow-orientation interaction.

Remark: In this article, we only resolve uniform cross-sectional orientation behavior. To leading order in the slender fiber approximation,² the uniaxial representation for \mathbf{Q} is given by

$$\mathbf{Q}(z, t) = s(z, t) \text{diag}[-1/3, -1/3, 2/3] \quad (9)$$

where $\text{diag}[-1/3, -1/3, 2/3]$ is a 3- \times -3 diagonal matrix. The scalar order parameter, $s(z, t)$, is identified with the normalized birefringence of a nematic uniaxial LCP melt^{3,14,18}:

$$s = \frac{\Delta n}{\Delta n_{\text{max}}} = \frac{1}{2} (3 \langle \cos^2 \theta \rangle - 1) \quad (10)$$

where $\langle \cdot \rangle$ represents an average over the orientation distribution function, θ is the angle between an individual molecule and the director, and Δn_{max} is the maximum birefringence determined by the values of the refractive indices parallel and perpendicular to the polymer chain. For TLCP fiber processes that are absent of difficulties such as spinline

breaks, the LCP is well approximated as a uniaxial nematic with director parallel to the fiber axis, and biaxiality is a very weak effect.³

Energy equation

$$\rho C \frac{dT}{dt} = \hat{\tau} : \mathbf{D} - \nabla \cdot \mathbf{q} \quad (11)$$

where C is the specific heat per unit mass and \mathbf{q} is the heat flux vector. The term $\hat{\tau} : \mathbf{D}$ models viscous heating. We follow Ziabicki,¹⁰ which is standard in the fiber literature, by neglecting the variation of internal energy and assuming that heat flux is due to conduction alone [eq. (20)]. We make no claims as to the global thermodynamic consistency of these assumptions.

Boundary Conditions

We adopt cylindrical coordinates (r, θ, z) , with the axial direction coincident with the direction of gravity and with orthonormal basis $\mathbf{e}_r, \mathbf{e}_\theta, \mathbf{e}_z$. The velocity is given by

$$\mathbf{v} = (v_r, 0, v_z) \quad (12)$$

where we assume $v_\theta = \mathbf{v} \cdot \mathbf{e}_\theta = 0$. This torsionless assumption is for simplicity and may be generalized to allow axisymmetric twist in the flow. The axisymmetric free surface is given by

$$F(r, z, t) = r - \phi(z, t) = 0 \quad (13)$$

At the fiber free surface, we have the kinematic boundary condition,

$$\frac{d}{dt} F = 0 \quad (14)$$

the kinetic boundary condition,

$$(\tau - \tau_a)\mathbf{n}_f = -\sigma_s \kappa \mathbf{n}_f \quad (15)$$

and the heat loss boundary condition

$$\mathbf{q} \cdot \mathbf{n}_f = -h(T - T_a) \quad (16)$$

In eqs. (15) and (16), τ_a and T_a denote the ambient stress and the ambient temperature at the fiber free surface, respectively; σ_s denotes the surface tension coefficient (assumed constant); \mathbf{n}_f is the unit outward normal vector of the free surface [eq. (13)]; κ is the mean curvature of the free surface; and h is

the heat loss coefficient, depending on processing conditions. In cylindrical coordinates,

$$\mathbf{n}_f = \frac{\mathbf{e}_r - \phi_{,z} \mathbf{e}_z}{(1 + \phi_{,z}^2)^{1/2}} \quad (17)$$

$$\kappa = \frac{1}{\phi(1 + \phi_{,z}^2)^{1/2}} - \frac{\phi_{,zz}}{(1 + \phi_{,z}^2)^{3/2}} \quad (18)$$

Here, “ $_{,z}$ ” denotes differentiation with respect to the axial coordinate z . We consider the heat loss coefficient to be a function of the local kinematic parameters [20],

$$h = \frac{k_\infty}{\phi} H \left(\frac{2\rho_\infty v \phi}{\mu_\infty} \right)^m \quad (19)$$

where k_∞ , ρ_∞ , and μ_∞ are the thermal conductivity, density, and viscosity of the ambient air at room temperature, respectively. The coefficients H and m are determined from experimental data. Other models for the heat transfer coefficient are available²¹; an extensive collection of the existing theoretical and empirical relationships between the Nusselt number and the Reynolds number for various flow situations can be found in Ziabicki's book.¹⁹ In this article, for simplicity, we vary the heat loss correlation exponent m in Eq. (19) to see the effect of heat transfer coefficient. Moreover, we use a Fourier law for the heat flux \mathbf{q} ,

$$\mathbf{q} = -K \nabla T \quad (20)$$

where K is the thermal conductivity.

The boundary ambient stress τ_a is expressed in the form

$$\tau_a = -(\hat{p} + p^a)\mathbf{n}_f - t^a \mathbf{m} \quad (21)$$

where

$$\mathbf{m} = \frac{\phi_{,z} \mathbf{e}_r + \mathbf{e}_z}{(1 + \phi_{,z}^2)^{1/2}} \quad (22)$$

is the unit vector tangent to the fiber-free surface in the rz plane. This form assumes axisymmetric air drag, with the normal and tangential components p^a and t^a functions of process conditions, in addition to a known constant barometric pressure \hat{p} . We use the empirical formula for the nondimensional tangential component of air drag

$$t^a = C_d \frac{(v \phi)^\gamma}{\phi^2} \quad (23)$$

where C_d is the air drag coefficient and γ is fitted from experimental data, $\gamma = 1.39$.²² We further assume that the normal component of air drag p^a is constant. Kase and Matsuo²³ included the effect of quench air flow normal to the fiber axis, and the final form is

$$t^a = C_d \frac{(v\phi)^\gamma}{\phi^2} \left[1 + 8 \left(\frac{v_a}{v} \right)^2 \right]^{1/6} \quad (24)$$

where v_a is the cross-flow velocity. In practice, v_a/v is less than .1, and the $1/6$ power of the term in brackets renders the expression very close to 1. In this article, we ignore cross-flow effects and only consider air drag given by eq. (23).

Asymptotic 1-D Model for TLCP Filaments

Upon nondimensionalizing the full set of 3-D equations in cylindrical coordinates (see refs. 2 and 3). The following collection of dimensionless parameters arises:

$$\begin{aligned} \epsilon &= r_0/z_0 & 1/W &= \sigma_s/\rho r_0 v_0^2 \\ N(T) & & \tilde{\alpha} &= 3ckT_{\text{melt}}/\rho v_0^2 \\ Pe &= \rho C z_0^2/Kt_0 & Bi &= h_0 r_0/K \\ \epsilon &= E/RT_{\text{melt}} & Es &= 2\eta_0 v_0/\tau_0 z_0 \\ \tilde{\eta}_0 &= \eta_0 t_0/\rho z_0^2 & 1/F &= gt_0^2/z_0 \\ \tilde{\lambda}_0 &= \lambda_0/t_0 & \sigma_d & \\ Br &= \eta_0 z_0^2/KT_{\text{melt}} t_0^2 & St &= h_0 z_0/\rho C v_0 r_0 \\ \tilde{\omega} &= \omega/T_{\text{melt}} & \Delta T &= 1 - T_a/T_{\text{melt}} \end{aligned} \quad (25)$$

Each of these parameters is important and carries physical information about the geometry, the flow, or the material rheology:

- $\tilde{\eta}_0$ represents the effective isotropic viscosity measured from the high temperature melt, whereas the Weber (W) and Froude (F) numbers, respectively, parametrize surface tension and gravity relative to inertia.
- $\tilde{\alpha}$ parametrizes the molecular kinetic energy per unit volume relative to inertial energy per unit volume.
- The combination $\tilde{\alpha}\tilde{\lambda}_0$ characterizes the relaxational stress due to molecular rotation relative to inertial stress.
- $\sigma_d(T)$ is the anisotropic drag parameter, and $\sigma_d/\tilde{\lambda}_0$ parametrizes anisotropic drag on poly-

mer molecular motion relative to the surrounding polymer molecules.

- $N(T)$ measures the strength of the intermolecular excluded-volume potential, whose shape in turn reflects the phase transition at a critical temperature, above which the unique equilibrium phase is isotropic and below which a stable nematic phase exists.
- Pe is the Peclet number, which is a measure of specific heat relative to thermal conductivity.
- Br is the Brinkman number describing viscous heating relative to thermal conductivity.
- Bi is the Biot number characterizing the heat loss relative to thermal conductivity.
- St is the Stanton number, which is the dimensionless heat transfer coefficient; notice that $Bi = St \cdot Pe \cdot \epsilon^2$.
- Es is the Ellis number describing the ratio of the effective viscosity to total stress.
- ϵ is the Griffith number quantifying the degree of effective isotropic viscosity variation with temperature.

Note that the characteristic temperature is chosen as the melt temperature.

- A nonisothermal parameter, ΔT , is introduced to measure the degree of nonisothermality. When $T_a = T_{\text{melt}}$, then $\Delta T = 0$ and our model reduces to the isothermal model of Forest, Wang, and Bechtel.³

Table I summarizes typical processing conditions and material parameters for LCP spinning processes; Table II defines the scales from which we nondimensionalize all equations. Table III contains a collection of all dimensionless parameters and typical values deduced from Tables I and II. The relative orders of these parameters guide the numerical studies that follow.

We vary the parameter ΔT to study the thermal effects on our previous isothermal LCP spin model predictions.³ Note that in dimensional units, the ambient temperature $T_a \equiv (1 - \Delta T)T_{\text{melt}}$. In simulations reported here, ΔT ranges from 0 (isothermal) to 0.5 because one should expect our model to be accurate only for small ΔT .

The following equations follow when all physical effects are presumed to couple at leading order except the Biot number, which must be $o(1)$ with respect to ϵ [e.g., $Bi \sim O(\epsilon^2)$]. This means the model derivation is formally valid only when there is weak

TABLE I
Process Parameters and Material Properties for
Typical LCP Melt Spinning Process

Process Parameters	Value
Spinline length	2 m
Radius $\phi(0)$ at $z = 0$	2×10^{-4} m
Velocity $v(0)$ at $z = 0$	0.5 m/s
Take-up velocity $v(1)$	$5 \sim 10$ m/s
Temperature $T(0)$ at $z = 0$	590 K
Ambient temperature T_a	300 K
Material Properties	Value
Melt density ρ	1300 kg/m ³
Effective isotropic viscosity η_0^\square	$0 \sim 10^3$ Pa · s
Thermal conductivity K	0.41 W/m · K
Glass transition temperature T_g	370 K
Specific heat C	1870 J/kg · K
$3ckT_{\text{melt}}^\dagger$	13000 Pa
Number of polymer molecules per unit volume c	5.3183×10^{23} /m ³
Dimensionless concentration N^+	4.17 ± 0.6
Surface tension σ_s	0.027 N/m
Relaxation time at melt temperature λ_0^*	$0.04 \sim 0.1$ s

[□]Many rheologists suggest $\eta_0 = 0$ for TLCPs. We propose that there must be an effective isotropic viscosity, analogous to that induced by the solvent for lyotropic LCPs.

[†]From Mori, Hamaguchi, & Nakamura.²⁷

⁺From Metzner & Prilutski.¹²

^{*}Adapted from Gregory.²⁸

Note: The data are from a Hoechst Celanese Report on Vectra A 910.

surface cooling relative to thermal conduction, which is the fundamental limiting factor in the application of 1-D nonisothermal slender models. This condition is not strictly satisfied along the entire spinline, so we are trading off the error in making this assumption for the significant numerical cost of

a full axisymmetric simulation.^{7,8} All other potentially small terms (e.g., $\frac{1}{Pe} \sim 10^{-6}$ from Table III) are retained and then explored later for a range of values to assess the influence of weak thermal conductivity. We give the minimum set of coupled equations that govern the leading order approximation of each unknown^{2,3}:

- ϕ —free surface radius
- v —axial velocity
- u —radial velocity
- p —pressure
- s —uniaxial nematic order parameter
- T —temperature

The 1-D model equations for axisymmetric TLCP filaments are

$$\left\{ \begin{array}{l}
 (\phi^2)_t + (v\phi^2)_z = 0 \\
 (\phi^2v)_t + (\phi^2v^2)_z = \frac{1}{F} \phi^2 + \frac{1}{W} \phi_z + (\phi^2 R_{\text{eff}}^{-1}(s, T) v_z + \alpha T U(s))_z - \beta v^\gamma \phi^{\gamma-1} \\
 s_t + v s_z = v_z (1 - s)(2s + 1) - \sigma_d \Lambda^{-1}(T) U(s) \\
 u = -v_z / 2 \\
 p = \frac{1}{W} \phi^{-1} - \tilde{\eta}_0 e^{\epsilon(1/T-1)} v_z - \frac{1}{3} \alpha T U(s) + \frac{2}{3} \alpha \Lambda(T) T s (1 - s) v_z \\
 T_t + v T_z = \frac{1}{Pe} \phi^{-2} (\phi^2 T_z)_z - 2 St \phi^{-1} [(v\phi)^m \phi^{-1}] (T - T_a) + \frac{Br}{Pe} [R_{\text{eff}}^{-1}(s, T) v_z + \alpha T U(s)] v_z
 \end{array} \right. \quad (26)$$

TABLE II
Scaling Factors for Numerical Simulations of the Process of Table I

Scale	Formula	Value
Radial length scale	$r_0 = \phi(0)$	2×10^{-4} m
Velocity scale	$v_0 = v(0)$	0.5 m/s
Axial length scale	$z_0 = \text{spinline length}$	2 m
Time scale	$t_0 = z_0/v_0$	4 s
Temperature scale	$T_{\text{melt}} = T(0)$	590 K
Stress scale	$\tau_0 = \eta_0 v_0/z_0$	32.5 ~ 40 Pa
Heat transfer scale	$h_0 = 1.352 \text{ J} \cdot \text{m}^{-1.667} \cdot \text{s}^{-0.667} \cdot \text{K}^{-1} \frac{v_0^{0.333}}{r_0^{0.667}}$	313.77 J/(m ² · s · K)

TABLE III
Dimensionless Numbers and Boundary Conditions for LCP Melt Spinning Process of Table I

Number	Formula	Value
Slenderness parameter	$\epsilon = r_0/z_0$	10^{-4}
Arrhenius viscosity parameter	$\mathcal{E} = E/(RT_{\text{melt}})$	$10 \sim 22$
Ellis number	$Es = 2\eta_0 v_0/(\tau_0 z_0)$	$1.6 \sim 2.5$
Froude number	$F = z_0/(gt_0^2)$	0.0127
Weber number	$W = \rho r_0 v_0^2/\sigma_s$	2.4
Effective isotropic viscosity	$\tilde{\eta}_0 = \eta_0 t_0/\rho z_0^2$	$0 \sim 0.7$
Stanton number	$St = h_0 z_0/(\rho C v_0 r_0)$	2.59
Biot number	$Bi = h_0 r_0/K$	0.1531
Peclet number	$Pe = \rho C z_0^2/(K t_0)$	5.9×10^6
Brinkman number	$Br = \eta_0 z_0^2/(K T_{\text{melt}} t_0^2)$	$0.13 \sim 0.165$
Drag coefficient	$C_d = 4.643 \times 10^{-6} \text{ Pa} \cdot \text{s}^{1.39} \cdot \text{m}^{-0.78} \frac{z_0 v_0^{1.39}}{\tau_0 r_0^{1.61}}$	$(8 \sim 9.8) \times 10^{-2}$
Anisotropic drag	$0 \leq \sigma_d \leq 1$	0.5
Polymer kinetic energy parameter	$\alpha = 3ckT_{\text{melt}}/(\rho v_0^2)$	40
Molecular relaxation parameter	$\tilde{\Lambda} = \lambda_0/t_0$	$0.025 \sim 0.1$
Arrhenius relaxation parameter	ω/T_{melt}	$11 \sim 25$
Dimensionless Boundary Conditions	Definition	Value
Upstream velocity	$v(0)/v_0$	1
Upstream average temperature	$T(0)/T_{\text{melt}}$	1
Downstream velocity (Draw ratio)	$v(1)/v(0)$	$10 \sim 20$
Dimensionless Temperatures	Definition	Value
Glass transition temperature	T_g/T_{melt}	0.62
Ambient temperature	T_a/T_{melt}	0.5

where $\gamma = 1.39$,²² $\beta = \frac{4C_d \tilde{\eta}_0}{Es}$, $\Lambda(T)$ is the scaled LCP relaxation time,

$$\Lambda(T) = \tilde{\Lambda} e^{\omega(1/T-1)} \quad (27)$$

$\tilde{\Lambda}$ is either a constant or proportional to $(1 - s^2)^2$, if the orientation dependence on rotary diffusivity is included¹⁷; $R_{\text{eff}}(s, T)$ is an effective 1-D flow-orientation Reynolds number,

$$R_{\text{eff}}^{-1}(s, T) = 3e^{\omega(1/T-1)} \tilde{\eta}_0 + 2\alpha T \Lambda(T) s^2 \quad (28)$$

consisting of an isotropic and an anisotropic contribution ($2\alpha T \Lambda(T) s^2$); and $U(s) = s(1 - N(T)/3(1 - s)(2s + 1))$ defines the uniaxial bulk free energy, $\int U(s) ds$. In Appendix A, we illustrate application of the isotropic and anisotropic stress contributions to fit experimental data on the commercial TLCP Vectra.

For transverse length and velocity scales, we choose the upstream values of fiber radius and axial velocity, and for axial length of the filament,

$$\begin{aligned} r_0 &\equiv \phi(z=0), \quad v_0 \equiv v(z=0), \\ z_0 &\equiv \text{spinline length} \end{aligned} \quad (29)$$

With these choices, the steady form of the equation of continuity (26)₁ integrates to

$$\phi^2 v = 1 \quad (30)$$

and the computational domain is scaled to $0 \leq z \leq 1$.

For steady states, if we select $m = 1/3$ in the heat loss coefficient form, then

$$h \sim (v\phi)^{1/3} \phi^{-1} = v^{1/3}/\phi^{2/3} = v^{2/3} \quad (31)$$

which is the form given by Matsui²⁴ and used by Henson et al.¹⁰. If we select $m = -1$, then

$$h \sim (v\phi)^{-1} \phi^{-1} = 1 \quad (32)$$

which corresponds to constant heat loss coefficient.

Note: From Table III, a realistic value for St is $O(1)$, $Pe^{-1} \sim O(\epsilon^{3/2})$, and the term $\frac{1}{Pe} \phi^{-2} (\phi^2 T_z)_z$ in eq. (26) could either be suppressed in the model or

kept as a small regularizing term. This approach in eq. (26) allows us to use one numerical code for all Peclet numbers. Later in this article, we study the effect of this weak conduction term for different values of Pe^{-1} ($Pe^{-1} = 1, 10^{-1}, 10^{-2}, 10^{-3}$, and 10^{-6}). The parameters in Table III are consistent with those in Metzner and Prilutski.¹²

Steady-State Solutions: Fiber Performance Predictions

Consistent with our earlier nondimensionalization, the upstream conditions on fiber radius, velocity, and temperature are fixed:

$$\phi(0) = 1, v(0) = 1, T(0) = 1 \quad (33)$$

The downstream thermal boundary condition assumes axial thermal conduction is negligible, that is,

$$\frac{\partial(\phi^2 T_z)}{\partial z}(1) = 0 \quad (34)$$

The remaining boundary conditions are free processing parameters to be specified/varied in the simulations that follow:

$$s(0), v(1) \quad (35)$$

The upstream degree of orientation, $s(0)$, is a function of spinneret design, whereas the take-up speed [$v(1) = \text{draw ratio} = Dr$] is a measure of process speed and throughput.

COMPARISON OF ISOTHERMAL AND NONISOTHERMAL SOLUTIONS

First, we highlight thermal effects on spun fibers. In Figure 1, we vary only the ambient temperature, $T_a = T_{\text{melt}}, 0.5T_{\text{melt}}$, respectively, and observe the following features:

- The velocity profile of the nonisothermal solution is consistent with experimental observations,^{6,19} quite distinct from the isothermal solution, clearly illustrating that thermal effects radically influence the qualitative hydrodynamic behavior.

- In the nonisothermal solution, the flow smoothly approaches a constant velocity as the temperature reaches the glass transition value. This confirms the one-phase model is self-consistent when the process parameters have been reasonably approximated.
- The steady process reaches the final degree of orientation very quickly in both cases. The final orientation, or birefringence, is significantly greater ($\sim 20\%$) in the nonisothermal case than in the isothermal case, indicating that cooling enhances molecular alignment.

Figure 2 shows the response of isothermal/thermal steady processes due to the gravity parameter (reciprocal Froude number), for $\frac{1}{Fr} = 0, 10, 100$, respectively.

- The isothermal solutions are very sensitive to the Froude number, whereas the thermal solutions are remarkably insensitive. This result confirms the industry practice to ignore effects of gravity in thermal spin models.
- Similar results are obtained if we vary the Weber number W (inversely proportional to surface tension), the air drag coefficient β , the effective isotropic viscosity at melt temperature $\bar{\eta}_0$, and the air drag exponent γ . That is, the isothermal steady states are sensitive to these parameter variations, whereas the nonisothermal are not. These observations may justify the omission of the relevant physical effects in the spinning model for steady-state simulations. However, they do have a nonnegligible impact on the realization of stable steady processes shown in the stability analysis that follows.
- The nonisothermal solution is also insensitive to the shape parameter for the short-range intermolecular potential $N(T)$. We have experimented with $N(T) \equiv 4$ and $N(T) = -1.5965 + 3.7232/T$ while all the other parameters are fixed as in Figure 1. Only negligible steady-state variations are observed however. This insensitivity to temperature changes in the short-range intermolecular potential underscores the dominant influence of elongational flow, in contrast with weaker shear flow.

Figure 3 shows the effect of orientation-dependent rotary diffusivity, eq. (7) or (27), on both isothermal and nonisothermal steady processes.

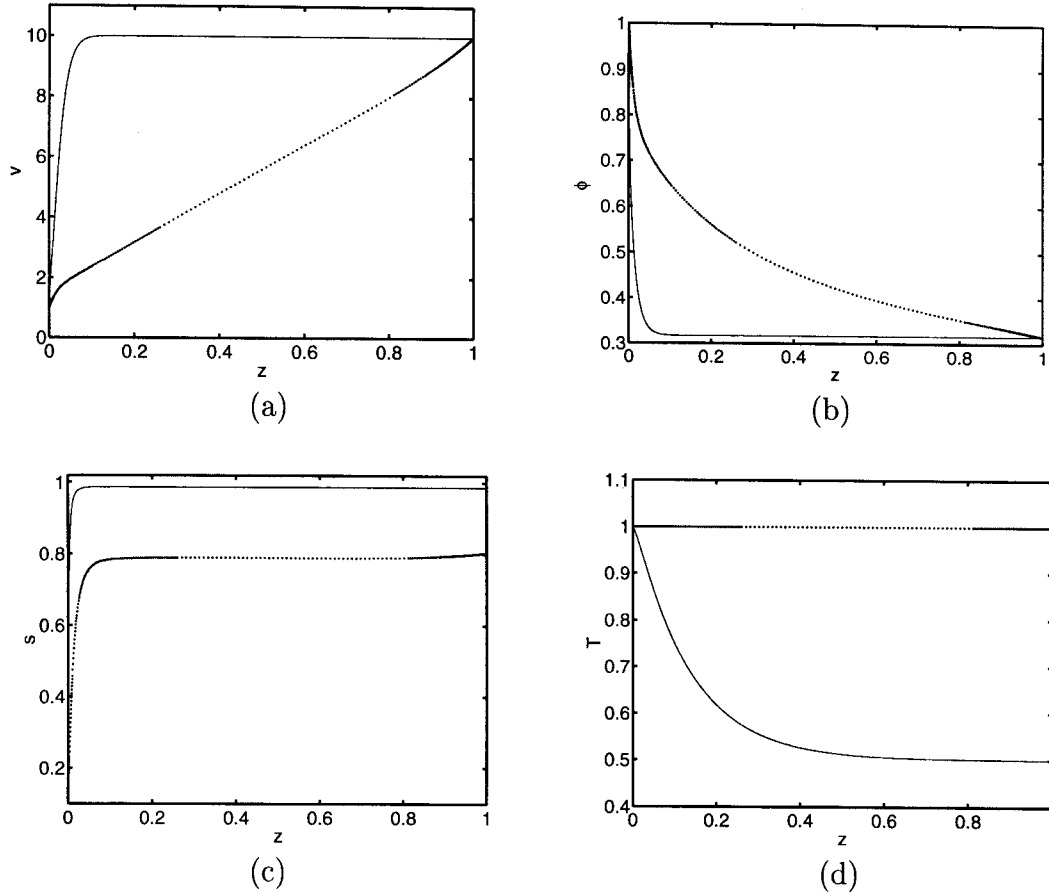


FIGURE 1. Isothermal (dotted) and nonisothermal (solid) steady spinning solutions, with $T_a = T_{\text{melt}}, 0.5T_{\text{melt}}$, respectively. All parameter values are chosen according to Table III with $\epsilon = 21$, $\omega = 16$, $\tilde{\eta}_0 = 0.125$, $\tilde{\Lambda} = 0.025$. For the figures to follow, these will be the default values unless specified. Boundary conditions are $\phi(0) = v(0) = T(0) = 1$, $s(0) = 0.1$, $v(1) = 10$.

- For the isothermal case, the effect is to accelerate the flow and reduce the orientation.
- For the nonisothermal case, the axial velocity, fiber radius, and temperature are insensitive to the coupling of orientation-dependent rotary diffusivity, whereas the final birefringence is decreased by approximately 10%.

THERMAL PROCESSES: EFFECTS OF HEAT CONDUCTION, HEAT LOSS, AND AMBIENT TEMPERATURE

Figure 4 shows the effect of Peclet number on nonisothermal solutions (recall that Pe is a measure of specific heat relative to thermal conductivity). A typical LCP melt has very high $Pe \sim O(10^6)$, Table III; the value $Pe = 10^3$ is plotted in Figure 4.

- All solutions are essentially unchanged with respect to variations of $Pe > 10^3$. Measurable process changes occur in the nonphysical range $1 \leq Pe \leq 10$.

Figure 5 exhibits the effect of the heat-transfer parameter m on nonisothermal solutions.

- With an increase in the heat transfer coefficient, the temperature naturally decreases faster. This results in a fiber that becomes thinner near the orifice and more aligned because of the temperature coupling to the effective Reynolds number [eq. (28)].
- The ambient temperature has a very significant effect on steady-state solutions (Figure 6). An increase in ΔT (i.e., a cooler ambient) leads to rapid temperature variations that couple to

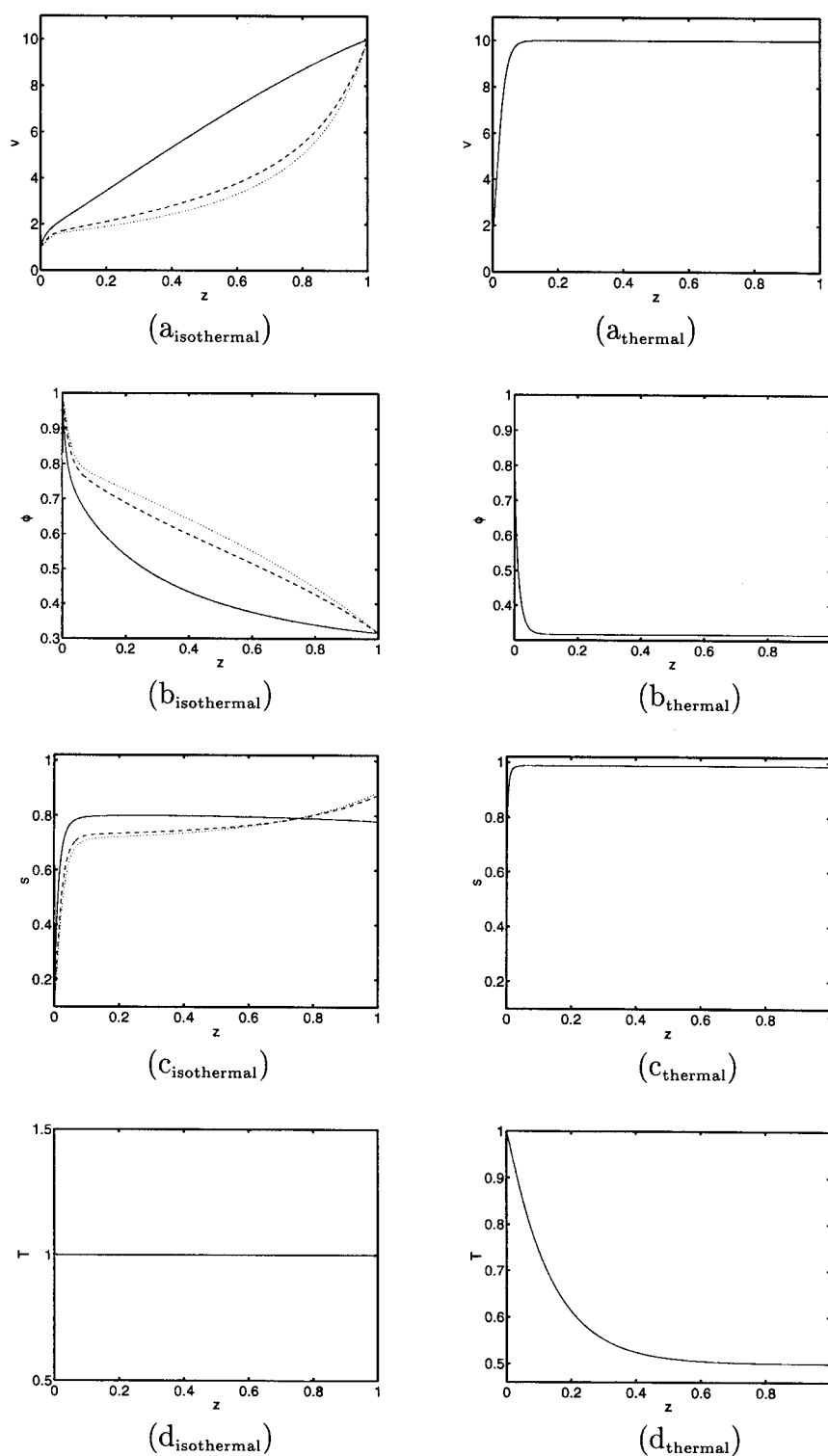


FIGURE 2. Sensitivity of isothermal versus thermal steady states due to changes of the gravity parameter (reciprocal Froude number), F^{-1} . Dotted curve, $F^{-1} = 0$; dashed curve, $F^{-1} = 10$; solid curve, $F^{-1} = 100$.

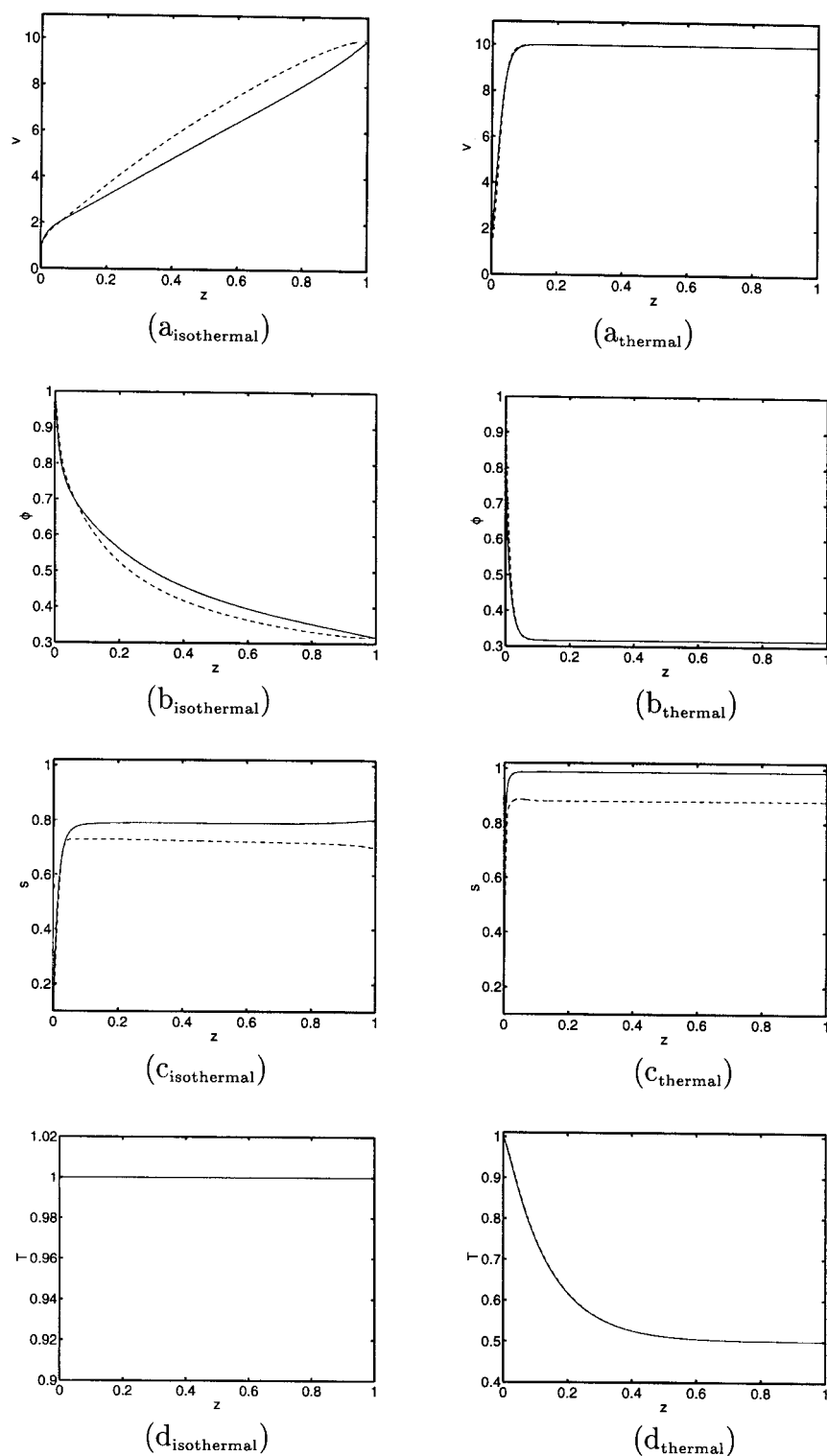


FIGURE 3. The effect of orientation-dependent rotary diffusivity on isothermal and nonisothermal solutions. Solid curves, without rotary diffusivity; dashed curves, with rotary diffusivity. All other parameter values are identical to Figure 1 with $\Delta T = 0.5$.

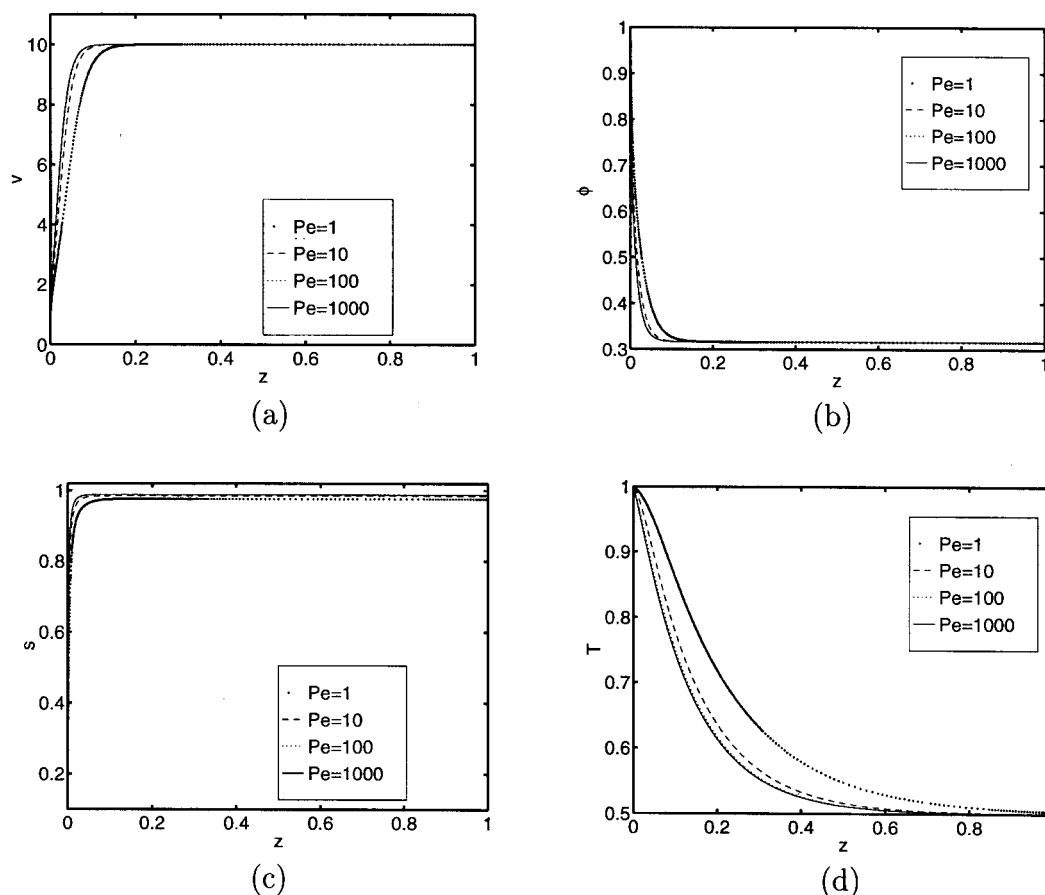


FIGURE 4. Effect of Peclet number Pe on nonisothermal steady spinning solutions where $T_{\text{ambient}} = 0.5 T_{\text{melt}}$. Increased Peclet number corresponds to a lower thermal conductivity at fixed specific heat.

the hydrodynamics through the effective Reynolds number [eq. (28)].

Figure 6 further suggests that *a cooler ambient results in a more oriented fiber*. This model prediction is consistent with industrial experience.

We note that this model yields lower orientation for cooler ambients when nonphysical parameters are specified. This amplifies the importance of accurate material and flow characterization before applying a mathematical model to real experiments.

EFFECT OF DRAW RATIO: NONISOTHERMAL MODEL SOLUTIONS AND SPUN FIBER PROPERTIES (BIREFRINGENCE, MODULUS, AND AXIAL FORCE)

Figure 7 depicts the effect of draw ratio Dr on nonisothermal processes. The draw ratio naturally

affects the axial velocity and radius of the fiber, whereas it has a much weaker effect on the nematic order parameter (birefringence) s and temperature.

We note from Figure 7 the agreement between our model predictions and experimental evidence^{6,13} of the effect of draw ratio Dr on spinline temperature at a fixed location. That is, the temperature at fixed locations slightly decreases at faster spinline speed. Our model does *not* yield this behavior in other parameter regimes that are unrelated to actual spinline data. This reversal of fiber response to a given process condition again underscores both the complexity of the fiber spinning physics and model equations [eq. (26)], and the importance of material characterization.

It is well known that molecular orientation affects many physical properties of natural and man-made fibers such as tensile strength and modulus. Therefore, a description of the dependence of final fiber orientation, $s(1)$, on draw ratio is important. Kuhn

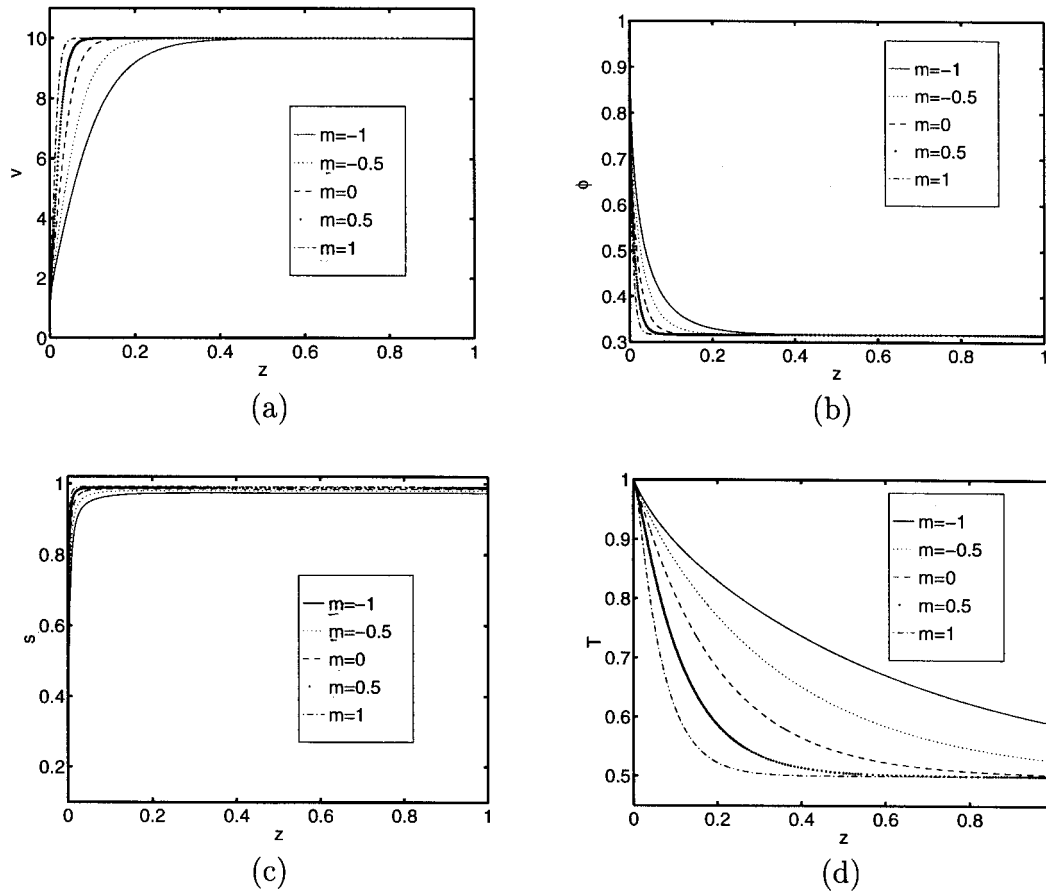


FIGURE 5. Effect of m , the heat loss correlation exponent in eq. (19), on nonisothermal steady spinning solutions where $T_{\text{ambient}} = 0.5 T_{\text{melt}}$.

and Grün²⁵ analyzed a system of rigid, asymmetric particles embedded in a medium of infinite viscosity. Starting with a random distribution of particles and assuming that their rotation is affine, they obtained an analytic relation between the *normalized birefringence* $s(1)$ and draw ratio Dr :

$$s(1) = \frac{2Dr^3 + 1}{2(Dr^3 - 1)} - \frac{3Dr^3}{2(Dr^3 - 1)^{3/2}} \operatorname{atan}[(Dr^3 - 1)^{1/2}] \quad (36)$$

This model has been used to infer birefringence in fiber spinning processes.¹⁴ We replace this “process–optical relation” by the solution of our TLCP spin model. The tradeoff is the solution of a boundary-value problem, which must be solved numerically, but for which we can predict response of the normalized birefringence, $s(1)$, to Dr (draw ratio) in

addition to all other material and process parameters.

In Figure 8a, we compare our predictions corresponding to two different spinneret values of orientation, $s(0)$, with the result given by eq. (36).

- The qualitative agreement between our spin model prediction and the Kuhn–Grün relation [eq. (36)] for normalized birefringence versus draw ratio is remarkable. Thus, trends in spinline performance are captured by eq. (36).
- Actual quantitative values of spun fiber birefringence cannot be captured by eq. (36) because translations of the curve occur due to other material or process conditions not resolved by this relation. For example, Figure 8a shows shifts in the relation due to spinneret values of orientation.

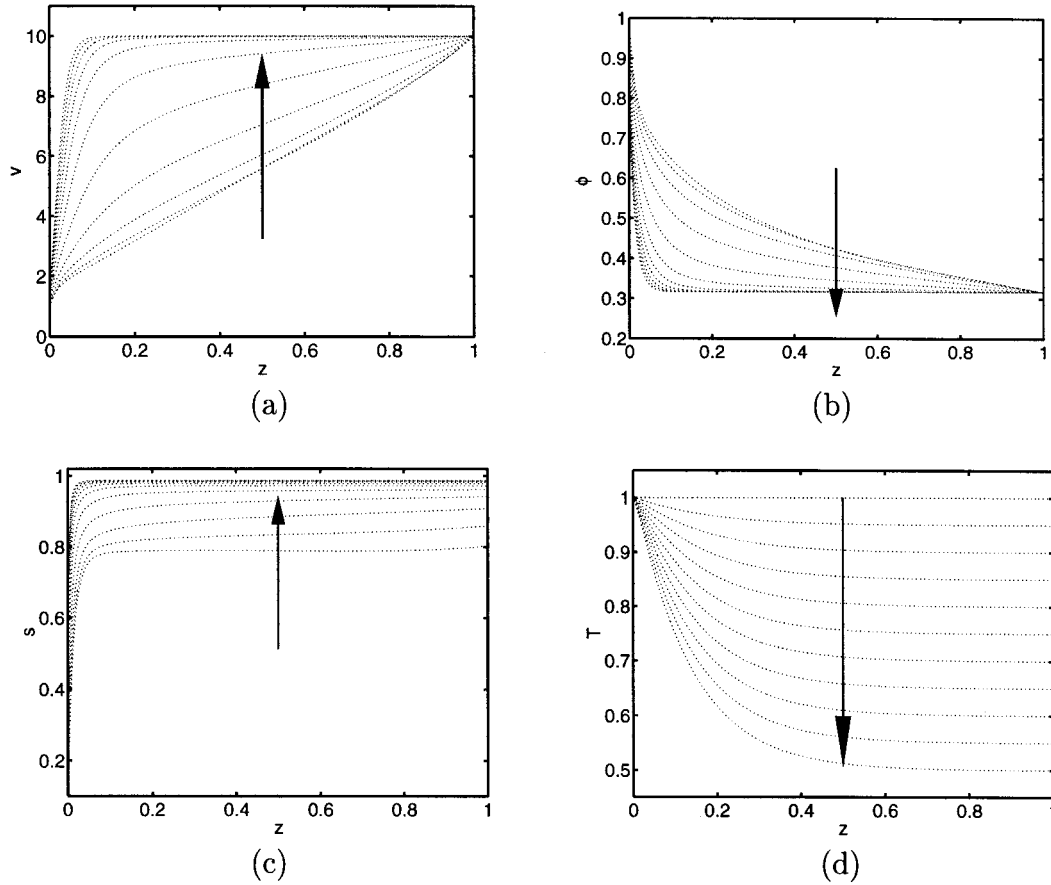


FIGURE 6. Steady solutions reflecting variations in the base state, Figure 1, due to changes in the ambient temperature T_{ambient} . We vary $\Delta T = 1 - T_{\text{ambient}}/T_{\text{melt}}$ from 0 (isothermal) to 0.5 in increments of 0.05. Arrows indicate the direction of increasing ΔT .

Picken *et al.*¹⁴ obtained an expression for an important performance property, the *fiber modulus* E , in terms of fiber birefringence $s(1)$ in the form

$$\frac{1}{E} = \frac{1}{e_3} + \frac{1}{3e_2} (1 - s(1)) \quad (37)$$

where e_3 is the chain modulus (approx. 240 GPa for PPTA) and e_2 is the shear modulus (approx. 2 GPa for PPTA). Using this relation, we calculate the modulus E as a function of draw ratio in Figure 8b. Our prediction agrees qualitatively with the result shown in Picken *et al.*¹⁴

In Figure 8c we plot the dimensionless *axial force at take-up*

$$F_{\text{axial}}(1) = \phi^2 \left[R_{\text{eff}}^{-1}(s, T) v_z + \alpha T U(s) - \frac{1}{W\phi} \right] \Big|_{z=1} \quad (38)$$

as a function of draw ratio Dr . The dimensional axial force is $F_{\text{axial}}(1)$ times the characteristic force, which is about 1.6×10^{-6} N from Table III. Notice that for small draw ratios less than 2.227, the axial force is negative. This is due to the presence of gravity, as explained in Appendix B. We remark that the constitutive-based relation [eq. (38)], when linearized about nearly isotropic nematics ($s \sim 0$), corresponds to a standard stress-optical law employed in the fiber industry for PET-like materials:

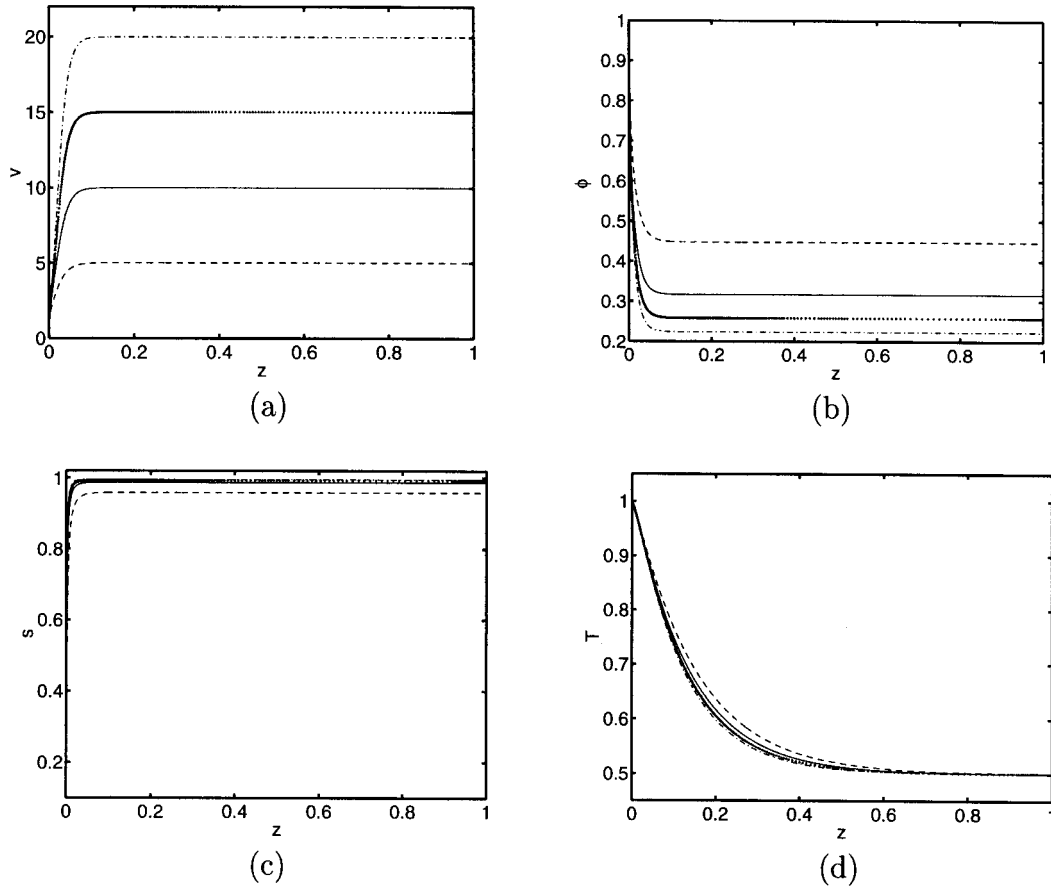


FIGURE 7. Effect of draw ratio Dr on nonisothermal steady spinning solutions where $T_{\text{ambient}} = 0.5 T_{\text{melt}}$. Dashed curves, $Dr = 5$; solid curves, $Dr = 10$; dotted curves, $Dr = 15$; dash-dot curves, $Dr = 20$.

$$\frac{\Delta n}{\Delta n_{\max}} = s = C_{\text{opt}} F_{\text{axial}}(1) + \hat{C} \quad (39)$$

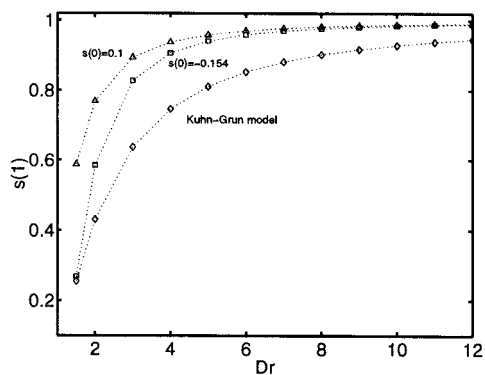
where \hat{C} is a translational constant.³

Material Bounds on Throughput: Linearized Stability of Steady-State Solutions

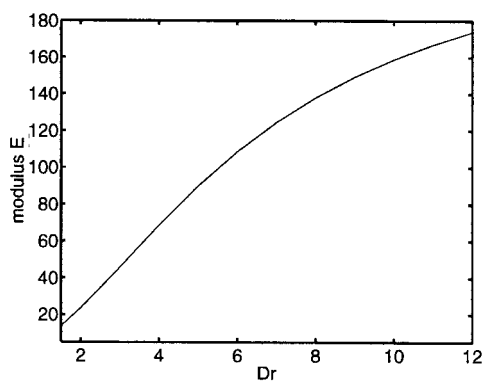
There are many process and material variables that make the spinning process unstable when some critical conditions are exceeded. Instability leads to irregular fibers or induces breakage of the individual filaments of the spinline. Hence, stability anal-

yses of steady-state solutions are very important. The traditional nonisothermal two-phase spin models do not have a continuous slope at the glass transition location, which prevents formulation of a linearized stability problem. However, the one-phase model we employ in this article allows us to perform a linearized stability analysis on steady-state solutions. In this section, we focus on linearized temporal stability of steady-state solutions by studying the *critical draw ratio* (the critical fiber spinning speed above which the process is linearly unstable) and its variation with respect to various process and material parameters.

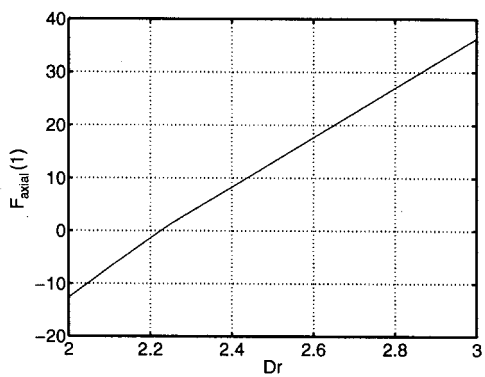
Figure 9a depicts the critical draw ratio Dr^* as a function of the ambient temperature, where all the material parameters are chosen according to Table III. For this parameter regime, the critical draw ratio de-



(a)



(b)



(c)

FIGURE 8. (a) Normalized fiber birefringence, $s(1)$, as a function of draw ratio, Dr . The top two curves correspond to our spin model predictions for two nearby values of upstream orientation, whereas the lower curve is the graph of the Kuhn–Grün relation that does not resolve dependence on $s(0)$. (b) Spun fiber modulus, E (units of GPa), as a function of Dr from the empirical formula of Picken [eq. (36)]. (c) Axial force at take-up as a function of Dr from the constitutive relations of our spin model.

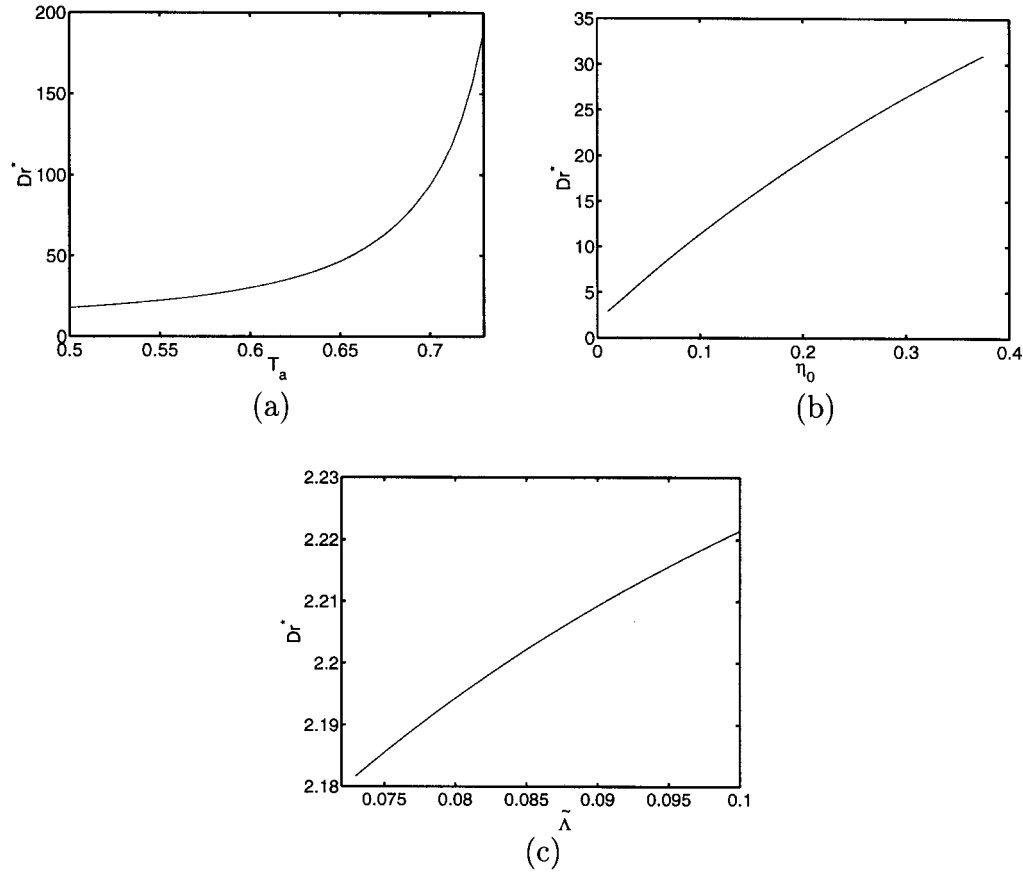


FIGURE 9. (a) The effect of the ambient temperature on critical draw ratio, Dr^* . (b) the Effect of the effective isotropic viscosity on critical draw ratio. (c) The effect of the relaxation time $\tilde{\Lambda}$ on critical draw ratio with $\tilde{\eta} = 0$, $\alpha = 4$, $\omega = 11$. In (b)–(c), the ambient temperature is fixed at 0.5 (i.e., $\Delta T = 0.5$).

creases with a cooler ambient. Combining Figure 9a with Figure 6, the model predicts that a cooler ambient yields increased birefringence, but lowers the maximum stable spinning speed. This competition among processing goals has to be balanced.

Now we fix the ambient temperature as shown in Table III and study the effects of various material parameters on the critical draw ratio. Our results are plotted in Figures 9b–d, 10, 11.

From Figure 9b, we determine that, as the effective isotropic viscosity parameter, $\tilde{\eta}_0$, decreases from 0.375 to 0.01, the critical draw ratio drops on order of magnitude, from 31 to 2.9. For nonisothermal LCP spinning, the effective isotropic viscosity is a primary material property that determines bounds on stable throughput. Recall that we have identified how this material property may be measured from a high-temperature melt viscosity experiment. Previous constitutive assumptions for TLCPs do not resolve

this isotropic stress contribution. To test whether this Doi constitutive model without isotropic viscosity can achieve higher stable draw ratios, in Figure 9c, we set the effective isotropic viscosity to zero, and then promote effective anisotropic viscosity by varying the relaxation parameter $\tilde{\Lambda}$. The critical draw ratio remains small. This parameter study indicates the need to retain a nonzero effective isotropic viscosity in the range $\tilde{\eta}_0$ between 0.1 and 0.2 to yield predictions consistent with industrial observations.

Figures 10 and 11 explore temperature-dependent rheological and heat transfer properties, respectively. All results suggest that strong thermal dependence limits stable throughput.

- Figure 10 shows lower throughput for increases in the TLCP kinetic energy parameter (α), Griffith number (ϵ , which models the rate

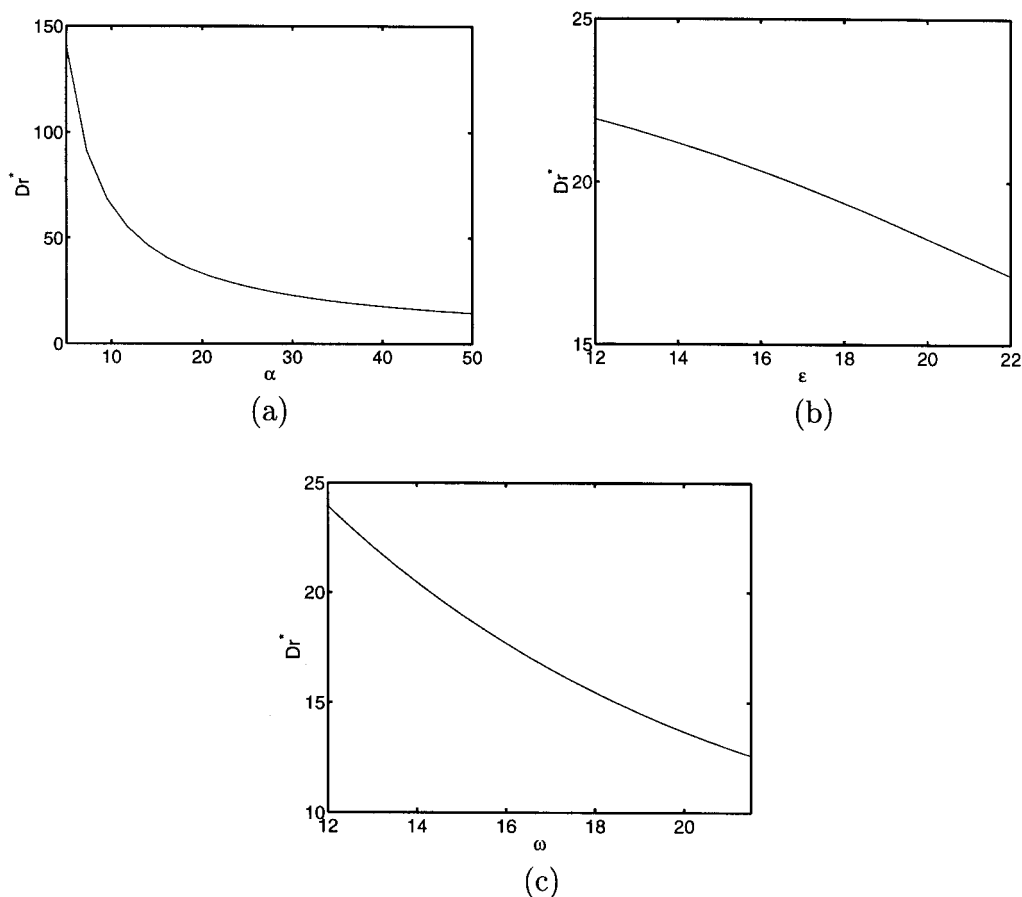


FIGURE 10. (a) The effect of α , the dimensionless molecular kinetic energy density, on critical draw ratio. (b) The effect of ϵ , the scaled activation energy, on critical draw ratio. (c) The effect of ω , the scaled LCP relaxation rate, on critical draw ratio. Here, the ambient temperature is fixed at 0.5 (i.e., $\Delta T = 0.5$).

of isotropic viscous hardening as the TLCP temperature drops down the spinline), and relaxation exponent (ω , which affects anisotropic viscous hardening as temperature drops).

- Figure 11a shows that in the range of weak thermal conductivity (high Pe), with all other conditions prescribed with realistic values, the critical draw ratio saturates at around $Dr^* \sim 13$.

Remark: The limit $Pe \gg 1$ is numerically very sensitive because it corresponds physically to transport (first-order derivatives) dominating conduction (second-order derivatives). We wanted to establish numerical convergence to confidently resolve the realistic, low con-

ductivity of TLCPs. To achieve convergence, an adaptive mesh refinement code²⁶ and iteration in Pe is necessary to accurately calculate these steady states and stability bounds.

- Figures 11b,c show that enhanced heat transfer, either from the heat loss coefficient (St) or exponent (m), lowers stable throughput.

Finally, we note that in realistic and processing parameter regimes, the critical draw ratio is insensitive to surface tension (W), gravity (F), and air drag coefficient (β). These results (not shown) are notable only because they are very important parameters for isothermal stability.³ Thus, thermal effects dominate these “hydrodynamic” effects.

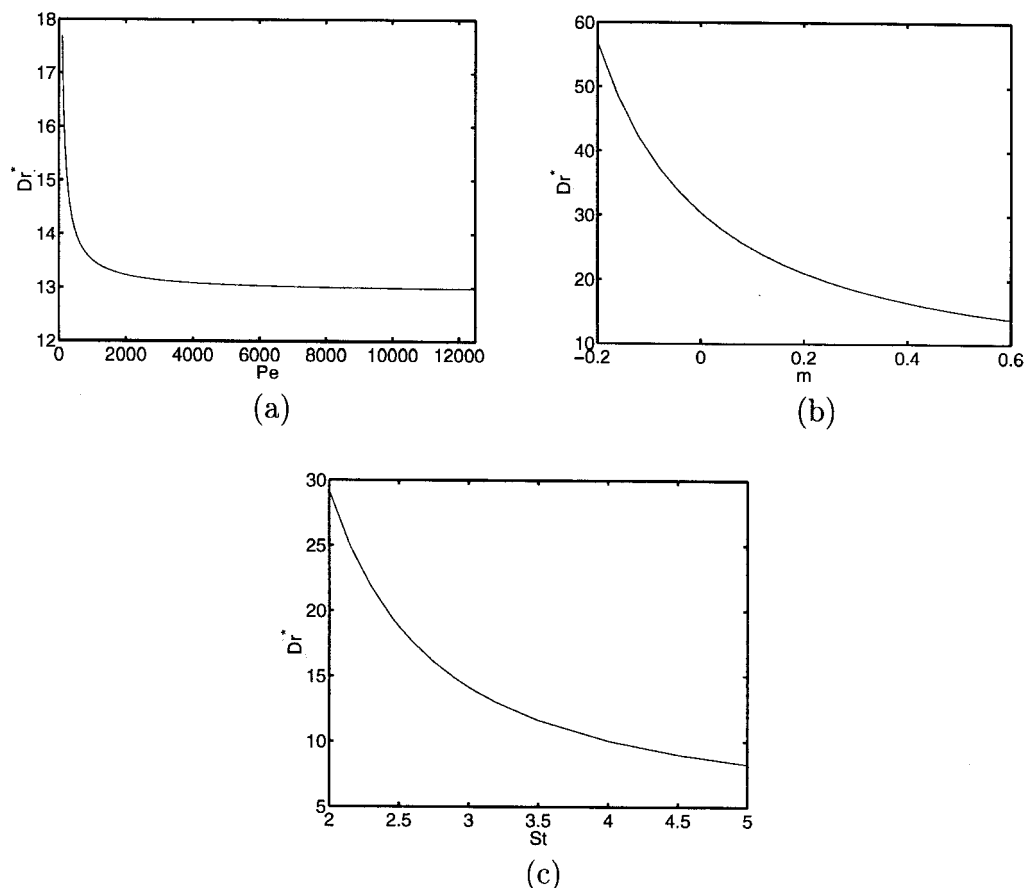


FIGURE 11. (a) The effect of the Peclet number, the specific heat relative to thermal conductivity, on critical draw ratio. (b) The effect of m , the heat loss correlation exponent, on critical draw ratio. (c) The effect of the Stanton number, dimensionless heat transfer coefficient, on critical draw ratio. Here, the ambient temperature is fixed at 0.5 (i.e., $\Delta T = 0.5$).

Conclusions

This study underscores some important points about spinning of TLCPs:

- Process stability has little correlation with qualitative dependence of steady states. In other words, there is no visible feature a process engineer might monitor as an indicator that the spinline is near critical.
- Some rheological properties, in particular the effective isotropic viscosity of the TLCP at melt temperature, are critical to process stability, which calls for further refinement in constitutive equations and experimental measurement by the rheology community.

- Trends in spinline performance due to material variations are often *reversed* in isothermal versus nonisothermal simulations. This result raises caution against application of isothermal models for real spinlines and emphasizes the critical role of thermodynamics in spinning processes.

Acknowledgments

Effort sponsored by the Air Force Office of Scientific Research, Air Force Materials Command, United States Air Force, under grant numbers F49620-97-1-0001, F49620-96-1-0131, and F49620-99-1-0003. The U.S. government is authorized to repro-

duce and distribute reprints for governmental purposes notwithstanding any copyright notation thereon. The views and conclusions contained herein are those of the authors and should not be interpreted as necessarily representing the official policies or endorsements, either expressed or implied, of the Air Force Office of Scientific Research or the U.S. government. The authors acknowledge the assistance of colleagues at Hoechst Celanese Corporation for providing publicly available TLCP spin data.

References

1. Ramalingam, S.; Armstrong, R. C. *J Rheol* 1993, 37(6), 1141–1169.
2. Forest, M. G.; Wang, Q.; Bechtel, S. E. *Physica D* 1997a, 99(4), 527–554.
3. Forest, M. G.; Wang, Q.; Bechtel, S. E. *J Rheol* 1997b, 41(4), 821–850.
4. Forest, M. G.; Ueda, T. *J Non-Newtonian Fluid Mechanics* 1999.
5. Bhave, A. V.; Menon, R. K.; Armstrong, R. C.; Brown, R. A. *J Rheol* 1993, 37, 413–441.
6. George, H. H. *Polym Eng Sci* 1982, 22, 292–299.
7. Vassilatos, G.; Schmelzer, E. R.; Denn, M. M. *Int Poly Proc* 1992, 7, 144–150.
8. Wang, Q.; Forest, M. G. In *Numerical Methods in Non-Newtonian Fluid Dynamics* (edited by G. C. Vradis and D. A. Siginer); ASME, New York, 1994.
9. Wang, Q.; Forest, M. G.; Bechtel, S. E. In *Developments in Non-Newtonian Flows* (edited by D. A. Siginer and S. E. Bechtel); ASME, New York, 1994.
10. Henson, G.; Cao, D.; Bechtel, S. E.; Forest, M. G. *J Rheol* 1988, 42(2), 329–360.
11. Forest, M. G.; Zhou, H.; Wang, Q. *SIAM J Appl Math* 1999.
12. Metzner, A. B.; Prilutski, G. M. *J Rheol* 1986, 30(3), 661–691.
13. Zieminski, K. F.; Spruiell, J. E. *J Appl Poly Sci* 1998, 35, 2223–2245.
14. Picken, S. J.; Northold, M. G.; van der Zwaag, S. In *Processing and Properties of Liquid Crystalline Polymers and LCP-Based Blends* (edited by D. Acierno and F. Mantia); 1995.
15. Huang, C. M.; Magda, J. J.; Larson, R. G. *J Rheol* 1999, 43(1), 31–50.
16. Walker, L.; Wagner, N. *J Rheol* 1994, 38, 1525–1547.
17. Doi, M.; Edwards, S. F. *The Theory of Polymer Dynamics*; Oxford University Press: Oxford, England, 1986.
18. Beekmans, F.; de Boer, A. P. *Macromolecules* 1996, 29, 8726–8733.
19. Ziabicki, A. *Fundamentals of Fibre Formation*; John Wiley & Sons: New York, 1976.
20. Kase, S.; Matsuo, T. *J Polym Sci A* 1965, 3, 2541–2554.

21. Huynh, B. P.; Tanner, R. I. *Rheol Acta* 1983, 22, 482–499.
22. Matsui, M. *Trans Soc Rheol* 1976, 20, 465–473.
23. Kase, S.; Matsuo, T. *J Appl Polym Sci* 1967, 11, 251–287.
24. Matsui, M. In *High-Speed Fiber: Science and Engineering Aspects*; Wiley-Interscience: New York, 1985.
25. Kuhn, W.; Grün, F. *Kolloid-Z* 1942, 101, 248.
26. Cash, J. R.; Wright, M. H. *SIAM J Sci Stat Comput* 1991, 12, 971–989.
26. Wang, Q. *J Rheol* 1997, 41, 943–970.
27. Mori, N.; Hamaguchi, Y.; Nakamura, K. *J Rheol* 1997, 41(5), 1095–1104.
28. Gregory, D. R. *J Appl Poly Sci* 1972, 16, 1479–1487.
29. Shah, Y. T.; Pearson, J. R. A. *Ind Eng Chem Fundam* 1972, 11(2), 145–148.
30. Shah, Y. T.; Pearson, J. R. A. *Ind Eng Chem Fundam* 1972, 11(2), 150–153.

Appendix A: An Experimental Confirmation of Constitutive Model for TLCPs

In simple shear flows of TLCPs with an imposed velocity field given by $(\mu y, 0, 0)$, the shear stress calculated from the constitutive relation [eqs. (3)–(6)], in which \mathbf{Q} has an explicit biaxial form² is

$$\mathbf{Q} = s \left(\mathbf{n}_2 \mathbf{n}_3 - \frac{\mathbf{I}}{3} \right) + \beta \left(\mathbf{n}_2 \mathbf{n}_2 - \frac{\mathbf{I}}{3} \right) \quad (40)$$

with order parameters (s, β) and directors \mathbf{n}_i , $i = 1, 2, 3$, given by

$$\tau_{xy} = \left[\eta(T) + \frac{3ckT\lambda(T,s,\beta)}{2} \left(1 - \frac{9(s - \beta)^2}{(2 + s + \beta)^2} \right) \left((s - \beta)^2 + \frac{1}{(3\sigma_d(T))} \right) \right] \mu \quad (41)$$

where μ is the shear rate. The effective isotropic viscosity and relaxation times are from eqs. (5) and (6):

$$\begin{aligned} \eta(T) &= \eta_0 e^{E/R(1/T - 1/T_0)} \\ \lambda(T) &= \lambda_0 e^{E/R(1/T - 1/T_0)} \end{aligned} \quad (42)$$

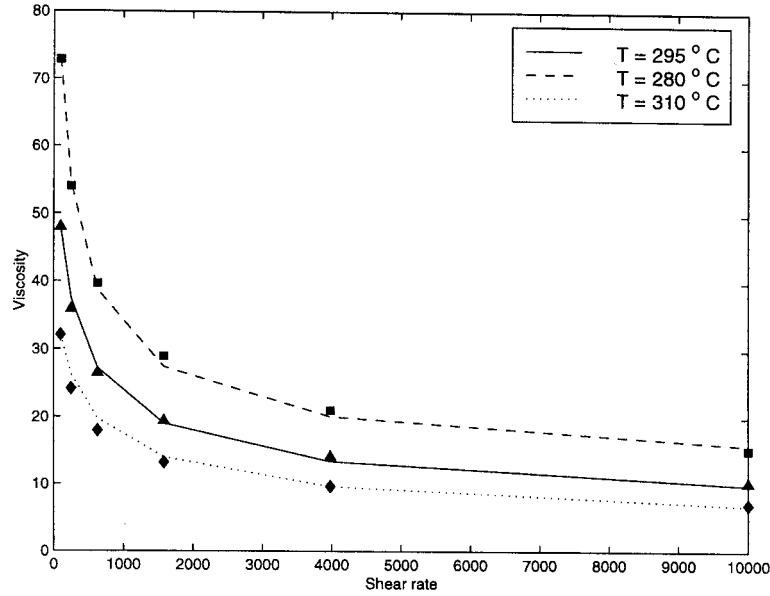


FIGURE 12. Comparison between the model prediction and experimental data. The symbols represent the experimental data, whereas the curves give the model predictions. The agreement is very good.

where $\omega = E/R$ is assumed. The effective shear viscosity is defined as [26]

$$\eta_{eff} = \frac{\tau_{xy}}{\mu} \quad (43)$$

given explicitly by

$$\eta_{eff} = \eta(T) + \frac{3ckT\lambda(T,s,\beta)}{2} \left(1 - \frac{9(s-\beta)^2}{(2+s+\beta)^2} \right) \left((s-\beta)^2 + \frac{1}{(3\sigma(T))} (2+s+\beta - (s-\beta)^2) \right) \quad (44)$$

where the order parameters (s, β) are solutions of the governing equation for the orientation tensor \mathbf{Q} in the shear flow field with respect to the given shear rate μ .

With the following parameter values,

$$\begin{aligned} \frac{E}{R} &= 6879.4 \text{ K}, 3ck = 89.0566 \text{ Pa/K}, \\ \eta_0 &= 3.1152 \text{ Pa} \cdot \text{s}, \lambda_0 = 0.01 \text{ s} \\ T_0 &= 583 \text{ K}, N = 4, \omega = \epsilon, \sigma_d = 1 \end{aligned} \quad (45)$$

we calculate the shear viscosity by first solving the orientation tensor equation [eq. (8)] at six given shear rates in accordance with the experimental

data for Vectra 910 (HCC report) and then using the formula [eq. (44)], with respect to three different values of temperature. Figure 12 plots the comparison between the model prediction and the experimental data for Vectra 910. The agreement is very good. This confirms that the use of the constitutive model for TLCP materials, such as Vectra 910, is plausible.

Appendix B: A Minimum Draw Ratio

Gravity accelerates the jet and can achieve a velocity beyond the take-up velocity somewhere in the spinline. Therefore, to satisfy the downstream boundary condition, the jet has to slow down near the take-up location, which can lead to a negative axial force. To see this more clearly, consider a free jet driven by gravity only. Then, one has

$$\frac{dv}{dt} = g \quad (46)$$

equivalently,

$$v(t) = gt + v(0) \quad (47)$$

To simplify the presentation, assume the jet reaches downstream with an average velocity defined here:

$$\langle v \rangle = \frac{v(0) + v(1)}{2} = \frac{1}{4} (1 + Dr) \text{ m/s} \quad (48)$$

using the data in Table III. Therefore,

$$\text{spinline length} = 2 \text{ m} = \langle v \rangle \cdot \text{total time} \quad (49)$$

and the total time it takes for the jet to reach downstream from upstream is

$$\text{total time} = \frac{8}{1 + Dr} \text{ s} \quad (50)$$

This gives the change of axial velocity from upstream to downstream

$$\Delta v = g \cdot \text{total time} = 9.8 \cdot \frac{8}{1 + Dr} \quad (51)$$

If $Dr = 1.5$, then $\Delta v = 31.36 \text{ m/s}$; if $Dr = 10$, then $\Delta v = 7.1272 \text{ m/s}$. To avoid deceleration of the jet, one needs

$$\Delta v \leq v(1) - v(0) = (Dr - 1) v(0) \quad (52)$$

Because $v(0) = 0.5 \text{ m/s}$, this condition with the help of eq. (51) yields

$$Dr \geq 12.56 \quad (53)$$

Hence, for a free falling jet, the downstream velocity has to be large enough to avoid negative axial force due to deceleration of the jet. In our more complex flow problem, the critical draw ratio is approximately 2.2.